Supplemental Material for "Diffusive Pseudo-Conformal Mapping: Anisotropy-Free Transformation Thermal Media with Perfect Interface Matching"

Gaole Dai,[1, *] Fubao Yang,[2] Jun Wang,[3, 4] Liujun Xu,[5, †] and Jiping Huang[2, ‡]

[1]*School of Sciences, Nantong University, Nantong 226019, China*

[2]*Department of Physics, State Key Laboratory of Surface Physics,*
and Key Laboratory of Micro and Nano Photonic Structures (MOE),
Fudan University, Shanghai 200438, China

[3]*School of Physics, East China University of*
Science and Technology, Shanghai 200237, China

[4]*School of Mathematics, East China University of*
Science and Technology, Shanghai 200237, China

[5]*Graduate School of China Academy of Engineering Physics, Beijing 100193, China*

————

[*] Electronic address: gldai@ntu.edu.cn

[†] Electronic address: ljxu@gscaep.ac.cn

[‡] Electronic address: jphuang@fudan.edu.cn

Note I: Analysis of interface matching: conformal, quasiconformal and pseudo-conformal mappings

To illustrate why conformal mappings are insufficient to design a heat flux guide, we need to resort to the theory of quasiconformal mapping [1]. In transformation optics, quasiconformal (or, more exactly, "extremal quasiconformal", "closest-to-conformal" or "most conformal" [2]) mappings are also used to reduce anisotropy [3–6]. Quasiconformal mappings are a common generalization of conformal mappings [1], but we will show that they also cannot match the interface flux. Thus, it is necessary to use pseudo-conformal mappings, which further relax the restrictions of conformal mappings compared with quasiconformal ones.

Now, take the heat flux guide as an example. The two simply connected regions with four endpoints $A_0 B_0 C_0 D_0$ [Fig. 1(a)] and $ABCD$ [Fig. 1(c)] on the boundaries are called topological quadrilaterals in the theory of quasiconformal mappings [1, 7]. A conformal mapping exits between them (Riemann mapping theorem [8]). However, this mapping does not necessarily match the two sets of endpoints one-to-one, e.g., $A_0 \to A$, $B_0 \to B$, $C_0 \to C$, and $D_0 \to D$. In fact, this correspondence is a basic requirement for designing a guide when considering interface matching, for example, maintaining the heat source settings. Achieving endpoints matching with conformal mappings requires that the two topological quadrilaterals belong to the same conformal equivalence class. They should have the same conformal module M, the aspect ratio of rectangles in the same equivalence class [1, 7]. When the two topological quadrilaterals have different conformal modules, only non-conformal mappings can make the endpoints match. In other words, non-conformal mappings shall change the conformal module.

Quasiconformal mappings are an important tool for dealing with endpoint matching. They satisfy the Beltrami equation [1]:

$$\frac{\partial f}{\partial \overline{z_0}} = \mu(z_0)\frac{\partial f}{\partial z_0}, \tag{S1}$$

where $\mu(z_0)$ is a complex value (named local complex characteristic) having a measure supremum: $|\mu| \leqslant k < 1$. It is evident that when $\mu(z_0)$ vanishes, the Beltrami equation reduces to the Cauchy-Riemann equation [Eq. (1)]. Figuratively speaking, the infinitesimal disk is still a disk under conformal mappings but becomes an ellipse under quasiconformal mappings. This is where anisotropy arises, and the local anisotropy can be measured by the

2

dilation or the aspect ratio of the ellipse [1]:

$$K(z_0) = \frac{1 + |\mu(z_0)|}{1 - |\mu(z_0)|}. \tag{S2}$$

In particular, quasiconformal mappings can make the change of conformal module bounded by a ratio range from $1/\sup|K(z_0)|$ to $\sup|K(z_0)|$, neither too large nor too small [1]. Quasiconformal ensures the existence of supremum $\sup|K(z_0)|$ for all z_0, i.e., the largest dilation in the domain.

One simple example of quasiconformal mappings is the affine transformation without changing the orientation. The affine transformation means the composition of a linear transformation and a translation:

$$f = Az_0 + B\overline{z_0} + C, \tag{S3}$$

and the preservation of orientation requires:

$$\left|\frac{\partial f}{\partial z_0}\right| > \left|\frac{\partial f}{\partial \overline{z_0}}\right| \quad \text{or} \quad |A| > |B|. \tag{S4}$$

Preserving orientation is also a necessary condition satisfied by all quasiconformal mappings. According to Grötzsch's theorem [1], the affine transformation is the closest to a conformal one among all the non-conformal mappings that match the endpoints of topological quadrilaterals. "Closet" means having the smallest $\sup|K(z_0)|$, i.e., extremal quasiconformal mapping. This can explain why affine transformations (for example, uniform compression/expansion on x_0 od y_0) are used in quasiconformal optical cloaks to minimize anisotropy [3–6]. In these works, the transformation can also be divided into two steps. An affine transformation is applied first to change the conformal module of the virtual space, and then a conformal mapping is used to obtain the optical cloak in the physical space [5, 6]. The composition transformation is usually not an affine one but still quasiconformal. A small constant diagonal anisotropy is generated in the first step which can finally be ignored if the cloak is much larger than the cloaked domain [6]. We can see that the requirement of preserving orientation is not necessary for ignoring anisotropy (e.g., $|A| < |B|$) since the major and minor axes of the ellipse can be swapped in the definition of dilation.

Further, only considering the endpoints is usually not enough for interface matching. As we have seen in the design of the heat flux guide, the expected transformation effect on interfaces $B_0C_0 \rightarrow BC$ and $A_0D_0 \rightarrow AD$ have been decided beforehand, which cannot be

3

realized if we use an affine transformation in the first step: $B_0C_0 \rightarrow B_1C_1$ and $A_0D_0 \rightarrow A_1D_1$ [Fig. 1]. Our method of pseudo-conformal mappings has a crucial difference from or generalization of quasiconformal mappings in the first step of non-conformal mappings. Pseudo-conformal mappings do not necessarily satisfy the Beltrami equation [Eq. (S1)]. In other words, they do not necessarily keep the orientation or have a finite $\sup |K(z_0)|$. The composition of one pseudo-conformal mapping and one conformal mapping is generally not a quasiconformal one, either. As long as pseudo-conformal mappings can induce diagonal anisotropy in a chosen coordinate system, we can remove the anisotropy if only one diagonal component of the conductivity tensor contributes to the flux. Here, diagonal anisotropy means pseudo-conformal mappings are angle-preserving for some (not all) sets of orthogonal grid lines. They can be Cartesian coordinates in the virtual spaces of the guide [Fig. 1(a)] and the cloaks [Fig. 4(a)], or the polar coordinates in the virtual space of the expander [Fig. 3(a)]. We can see that the uniform compression/expansion is also a pseudo-conformal mapping. Below we discuss the specific form of this diagonal anisotropy and how it can be equivalent to an isotropic parameter. We still consider an isotropic virtual space. The governing equation [Eq. (2b)] in Cartesian coordinates is

$$\nabla_0 \cdot (\kappa_0 \nabla_0 T_0) = \frac{\partial}{\partial x}\left(\kappa_0 \frac{\partial T_0}{\partial x}\right) + \frac{\partial}{\partial y}\left(\kappa_0 \frac{\partial T_0}{\partial y}\right) = 0. \tag{S5}$$

More generally, we can select a corresponding orthogonal coordinate system according to the isotherm-streamline grid lines in the virtual space. Of course, we have different choices for the mapping from isotherms and streamlines to 2D spatial coordinates denoted by (q^1, q^2). In particular, an intuitive way is to take one of the coordinates linearly related to the temperature. Nevertheless, the difference in the assignment of coordinates does not affect the final conclusion about the transformation rule of thermal conductivity. Eq. (2b) in orthogonal contravariant coordinates (q^1, q^2) is

$$\nabla_0 \cdot (\kappa_0 \nabla_0 T_0) = \frac{1}{h_1 h_2}\frac{\partial}{\partial q^1}\left(\frac{h_2}{h_1}\kappa_0 \frac{\partial T_0}{\partial q^1}\right) + \frac{1}{h_1 h_2}\frac{\partial}{\partial q^2}\left(\frac{h_1}{h_2}\kappa_0 \frac{\partial T_0}{\partial q^2}\right) = 0, \tag{S6}$$

where h_i is the scale factor. When considering a pseudo-conformal mapping, streamlines and isotherms in the virtual space are mapped onto another set of orthogonal streamlines and isotherms in the physical (or the auxiliary) space. Denote this set of orthogonal contravariant coordinates as (u^1, u^2). The corresponding governing equation [Eq. (2a)] in (u^1, u^2) in the physical space must have the same form as Eq. (S6) or simply as Eq. (S5) for the guide and

4

the cloaks. Eq. (2a) in general curvilinear coordinates (u^1, u^2) is

$$\nabla \cdot (\boldsymbol{\kappa} \cdot \nabla T) = \frac{1}{\sqrt{g}} \frac{\partial}{\partial u^i} \left(\sqrt{g} \kappa^{ij} \frac{\partial T}{\partial u^j} \right) = 0, \tag{S7}$$

where g is the determinant of $g_{ij} = \mathbf{g}_i \cdot \mathbf{g}_j$ ($\mathbf{g}_i$ is the covariant basis) and κ^{ij} is the contravariant component of $\boldsymbol{\kappa}$. Due to the form-invariance and the orthogonality, Eq. (S7) can reduce to

$$\nabla \cdot (\boldsymbol{\kappa} \cdot \nabla T) = \frac{1}{L_1 L_2} \frac{\partial}{\partial u^1} \left(L_1 L_2 \kappa^{11} \frac{\partial T}{\partial u^1} \right) + \frac{1}{L_1 L_2} \frac{\partial}{\partial u^2} \left(L_1 L_2 \kappa^{22} \frac{\partial T}{\partial u^2} \right) = 0, \tag{S8}$$

and the thermal conductivity in the physical space can be expressed as

$$\boldsymbol{\kappa} = \kappa^{ii} \mathbf{g}_i \otimes \mathbf{g}_i = \kappa^{ii} L_i^2 \hat{\mathbf{g}}_i \otimes \hat{\mathbf{g}}_i. \tag{S9}$$

Here, $\hat{\mathbf{g}}_i = \mathbf{g}_i / L_i$ is the normalized basis, and $L_i = |\mathbf{g}_i| = \sqrt{g_{ii}}$ is the scale factor. We can see $\boldsymbol{\kappa}$ is diagonalized in orthogonal coordinates (u^1, u^2), which means the tangents of grid lines, i.e., the basis vectors $\hat{\mathbf{g}}_i$, are just the principal axes at each point. Based on Eqs. (S6) and (S8), we can obtain the contravariant component of $\boldsymbol{\kappa}$:

$$\kappa^{11}(z) = \frac{1}{L_1(z)L_2(z)} \frac{h_2(z_0)}{h_1(z_0)} \kappa_0(z_0), \quad \kappa^{22}(z) = \frac{1}{L_1(z)L_2(z)} \frac{h_1(z_0)}{h_2(z_0)} \kappa_0(z_0). \tag{S10}$$

When talking about the principal values or eigenvalues of $\boldsymbol{\kappa}$, we actually focus on the value of $\kappa^{ii} L_i^2$:

$$\kappa^{11} L_1^2 = \frac{L_1}{L_2} \frac{h_2}{h_1} \kappa_0, \quad \kappa^{22} L_2^2 = \frac{L_2}{L_1} \frac{h_1}{h_2} \kappa_0. \tag{S11}$$

In the physical space, there is also a set of orthogonal coordinates denoted by $(\underline{q}^1, \underline{q}^2)$ which use the same grid lines as (q^1, q^2) in the virtual space. The Jacobian J_f for the complex transformation $z_0 \mapsto z$ in the main text is both the Jacobian of the coordinate transformation $(u^1, u^2) \mapsto (\underline{q}^1, \underline{q}^2)$ in the physical space and the push-forward derivative of diffeomorphism expressed by $(q^1, q^2) \mapsto (\underline{q}^1, \underline{q}^2)$ from the virtual space to the physical space. It determines the value of L_1/L_2 with $L_i(z)/h_i(z) = \sqrt{\mathrm{J}_f^\top \mathrm{J}_f}$. Our two-step approach splits the effect of coordinate transformations on thermal conductivity into two parts as well. In our first steps for the three applications in the main text, they correspond to a kind of geometric transformation $(q')^i = (q')^i(q^i)$ written in the same coordinate system for two spaces. It induces a diagonal Jacobian since it maps the curve of constant-q^i in one space to the curve of constant-$(q')^i$ in another space, and we only consider the case where $\frac{\partial (q')^i}{\partial q^i} > 0$ is satisfied. The second step is a conformal mapping and does not change L_1/L_2 at each point. At last, we have

$$\frac{L_1(z)}{L_2(z)} \frac{h_2(z)}{h_1(z)} = \frac{\partial (q')^1}{\partial q^1} \Big/ \frac{\partial (q')^2}{\partial q^2}. \tag{S12}$$

When $\frac{\partial T}{\partial u^2}$ vanishes in Eq. (S8), it is easy to check that an isotropic thermal conductivity

$$\kappa(z) = \kappa_0 \left(\frac{\partial(q')^1}{\partial q^1} / \frac{\partial(q')^2}{\partial q^2} \right) \frac{h_1(z)}{h_1(z_0)} \frac{h_2(z_0)}{h_2(z)} \quad (S13)$$

can induce the same thermal fields as the anisotropic $\boldsymbol{\kappa}$ by requiring $\frac{L_2}{L_1}\kappa = L_1 L_2 \kappa^{11}$. We can see κ in Eq. (S13) is just the first diagonal element $\kappa^{11}L_1^2$ in Eq. (S11). If we instead map the isotherm originally labeled by q^1 to a new coordinate $\tilde{q}^1$ in the virtual space ($\partial\tilde{q}^1/\partial q^1 > 0$), the corresponding scale factor is $\tilde{h}_1 = h_1 \partial q^1/\partial\tilde{q}^1$. A similar operation can be done for the streamlines to use the new coordinate. Now, the first-step pseudo-conformal mapping writes $(\tilde{q}')^i = (\tilde{q}')^i(\tilde{q}^i)$. Since $\frac{\partial(q')^i}{\partial q^i} = \frac{\partial(q')^i}{\partial(\tilde{q}')^i} \frac{\partial(\tilde{q}')^i}{\partial\tilde{q}^i} \frac{\partial\tilde{q}^i}{\partial q^i}$, mapping the isotherm-streamline grids to different coordinate values in virtual space does not affect the thermal conductivity [Eq. (S13)] in the physical space.

Finally, we should point out that the terminology "pseudo-conformal mapping" sometimes might refer to "biholomorphic mapping" (a generalization of univalent conformal mapping with several complex variables) [8] in early studies. However, this usage is quite uncommon now, especially in English literature. Without causing ambiguity, we can call our method "pseudo-conformal" to denote a further generalization of quasiconformal mappings.

Note II: Experimental demonstration of the heat flux guide

In experimental verification for the heat flux guide, the required κ distribution is approximately realized by a sample made of copper-air composites. In the top view [Fig. S1(a)], the sample and the model in the simulation [Fig. 2] have the same size, except for a slight extension (0.6 cm each) at both ends (i.e., the inlet and outlet). The matrix material of the guide is copper, engraved with 20×30 periodic air holes. The guide part of the sample is a one-twelfth annulus whose inner and outer radii are 40 cm and 60 cm, respectively. The background part has a length of 10.74 cm. The air-hole array is formed by rotating the bottom row (containing 20 holes) about the origin: starting from a rotation of 1° and ending with a rotation of 29°, with periodic intervals of 1°. In the 3D view [Fig. S1(b)], the copper plate and the air cylinders are 0.3 cm thick. Two aluminum plates (8 cm long) screwed to the copper extensions are inserted into the water baths. The thermal conductivities of copper and aluminum are 400 W m^{-1} K^{-1} and 273 W m^{-1} K^{-1}, respectively.

In particular, the bottom row of air holes is shown in Fig. S1(a). It is divided into 20 parts
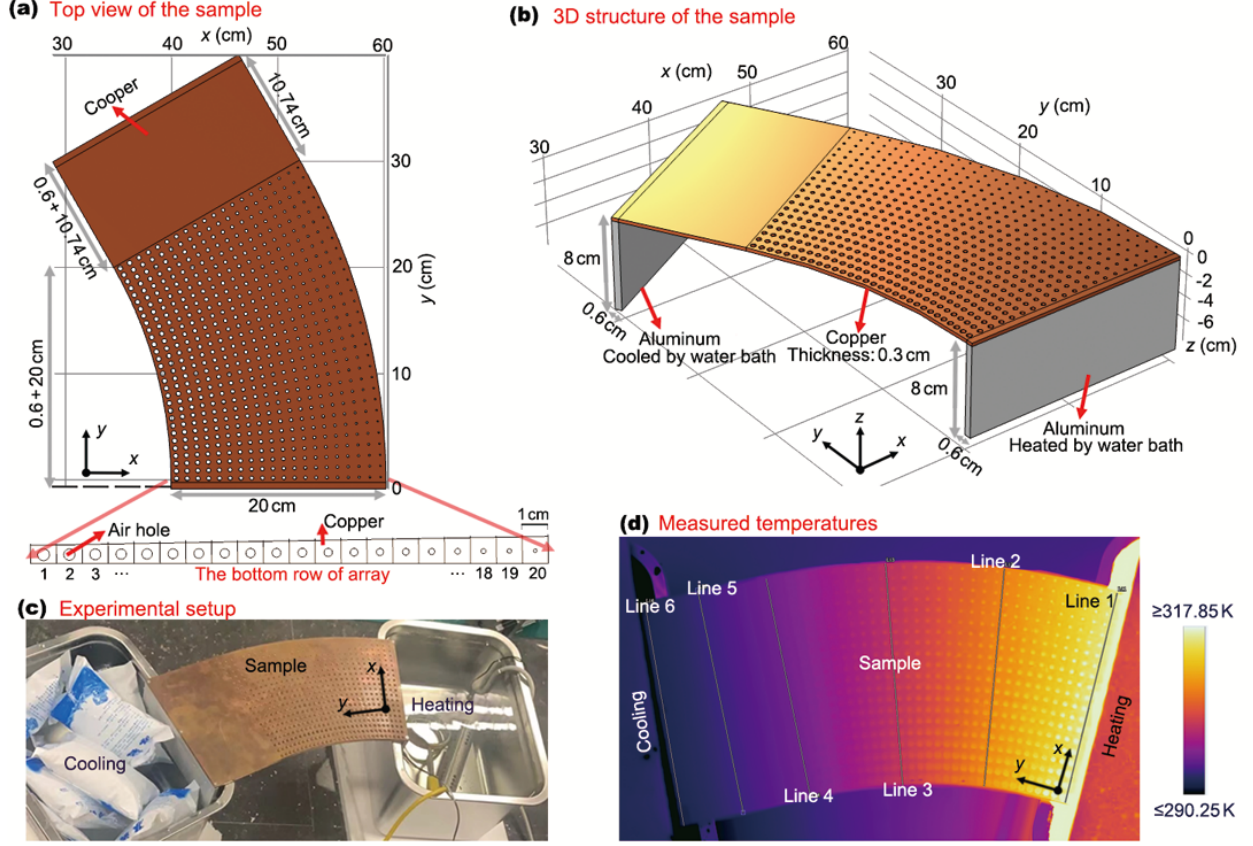
FIG. S1: Experimental demonstration of a thermal guide. (a) Structure of the guide: top view. The structure is composed of copper (dark color) and air (white holes) (b) 3D structure of the guide. (c) Photograph of the experimental setup. (d) Measured temperature distributions.

according to the rotation trajectory of the twentieth points on the inlet, each containing an air hole labeled by sequence number n from 1 to 20. The centers of these holes are on the constant-azimuth line with regard to 0.5°, and their radial coordinates are $(39.5 + n)$ cm. The radii of the air holes r_n are determined based on the effective medium approximation. Each part in the bottom row (also labeled by n) is expected to have an effective thermal conductivity κ_n equal to the spatial average calculated by Eq. (4), which is approximately $6.5 \times (39.5 + n)$ W m^{-1} K^{-1}. Thermal conductivities of the air and the copper are denoted by κ_{air} and κ_{Cu}, respectively. The volume fraction of the air hole in each part of the bottom row, f_n, equals $360 r_n^2/(79 + 2n)$ (r_n in cm). Then, we have the Maxwell-Garnett formula [9]:

$$\frac{\kappa_e - \kappa_{Cu}}{\kappa_e + \kappa_{Cu}} = f_n \frac{\kappa_{air} - \kappa_{Cu}}{\kappa_{air} + \kappa_{Cu}}, \tag{S14}$$

and the values of r_n can be obtained and listed in TABLE I. For simplicity, we take $\kappa_{air} \approx 0$

in calculation.

<table>
<tr><td colspan="8" align="center">TABLE I: Radii of the air holes.</td></tr>
<tr><td>Sequence number n</td><td>1</td><td>2</td><td>3</td><td>4</td><td>5</td><td>6</td><td>7</td></tr>
<tr><td>Radius r_n (cm)</td><td>0.23</td><td>0.22</td><td>0.21</td><td>0.20</td><td>0.20</td><td>0.19</td><td>0.19</td></tr>
<tr><td>Sequence number n</td><td>8</td><td>9</td><td>10</td><td>11</td><td>12</td><td>13</td><td>14</td></tr>
<tr><td>Radius r_n (cm)</td><td>0.18</td><td>0.18</td><td>0.17</td><td>0.17</td><td>0.16</td><td>0.15</td><td>0.14</td></tr>
<tr><td>Sequence number n</td><td>15</td><td>16</td><td>17</td><td>18</td><td>19</td><td>20</td><td></td></tr>
<tr><td>Radius r_n (cm)</td><td>0.13</td><td>0.12</td><td>0.11</td><td>0.10</td><td>0.09</td><td>0.07</td><td></td></tr>
</table>

Fig. S1(c) is a photo of the experimental setup in our lab. On the left of the sample is an ice-water mixture (cooling) and on the right is another water bath with a heating rod. When the experimental setup reaches a steady state, a temperature difference of about 25 K can be generated between the two ends of the guide. Fig. S1(d) shows the measured temperature distribution detected by an infrared camera. The six lines corresponding to their counterparts in Fig. 2(b) are also plotted. The temperature data read from them are shown in TABLE II. The first three rows show the number of data points, average temperature and standard deviation on each line. The last three rows correspond to the data after the extreme values of the edges are discarded. Due to the way they come into contact with the water baths, the sample is not strictly isothermal at both ends. The error also comes from the influence of the environment (loose thermal insulation boundaries) and the approximation of the sample itself relative to the ideal parameters. The difference between the two groups of data in the middle four lines is relatively small. The extreme values on the outlet and inlet have a more significant impact. The copper and aluminum plates are tightened with screws on the four endpoints, which increases the interfacial thermal resistance. In addition, the temperature difference from the environment is the greatest here because of the closest distance to water baths.

TABLE II: Measured temperatures on the six chosen lines in Fig. S1(d).

Data line	1	2	3	4	5	6
Number of data	259	268	272	272	276	276
Average temperature (K)	316.91	308.92	302.37	297.10	294.63	292.01
Standard deviation (K)	1.16	0.41	0.19	0.12	0.14	0.47
Number of data[a]	233	240	244	244	248	248
Average temperature[a] (K)	316.68	308.94	302.37	297.10	294.65	292.10
Standard deviation[a] (K)	0.38	0.40	0.17	0.11	0.09	0.38

[a] The extreme data with an arc length of 1 cm at both ends are discarded.

Note III: Detailed derivations of finding the appropriate pseudo-conformal mapping for the expander

To obtain the thermal conductivity in Eq. (5), we use an auxiliary space whose polar coordinates are radius r and azimuth ψ. Again, a pseudo-conformal mapping $z_0 = \rho e^{i\theta} \mapsto z_1 = r e^{i\psi}$ is first applied from the virtual space to the auxiliary one. Then, the Möbius transform $z = i\frac{i+re^{i\psi}}{i-re^{i\psi}}$ shapes the expander in the physical space. To homogenize the heat flux, we need to rearrange the streamlines labeled by θ so they can cut the x-axis (an interval-length equal to 2) evenly in the physical space (a constant $\partial x/\partial \theta$). To do so, the pseudo-conformal map can be simplified as $\theta \mapsto \psi \in [\pi, 2\pi]$, and it maps the lower unit half-disk onto itself. Since the Möbius transform gives $x = \frac{\cos \psi}{1-\sin \psi}$ on the x-axis, we should require

$$\frac{\partial x}{\partial \psi}\frac{\partial \psi}{\partial \theta} = \frac{\partial \psi}{\partial \theta}\frac{1}{1-\sin \psi} = \frac{2}{\pi}. \tag{S15}$$

It is easy to find the inverse mapping $\psi \mapsto \theta$ is

$$\theta = \frac{\pi}{2}\frac{\cos \psi}{1-\sin \psi} + \frac{3}{2}\pi. \tag{S16}$$

The analytical expression of $\psi = \psi(\theta)$ is

$$\psi = 2\arctan\left(\frac{\theta - 2\pi}{\theta - \pi}\right) + 2\pi. \tag{S17}$$

In fact, we only need to know the Jacobian element $J_{\psi\theta} = \frac{2}{\pi}(1-\sin \psi)$ since we do not need to transform the coordinate ρ. Then, the thermal conductivity in the auxiliary space

is (recalling Eq. (7))

$$\kappa_1 = \frac{\rho}{r}\frac{\mathrm{J}_{r\rho}}{\mathrm{J}_{\psi\theta}} = \frac{\pi}{2}\frac{1}{1-\sin\psi}\kappa_0 \tag{S18}$$

because only κ_1^{rr} (or $\kappa_0^{\rho\rho}$) appears in the heat conduction equation in the auxiliary (or virtual) space. Based on Eq. (3b), the point source power should be $Q_0/(2\mathrm{J}_{\psi\theta}(\rho=0))$ to ensure $T(z) = T_0(z_0(z))$. Since different power values will not change the family of curves of isotherms, we can still take $Q = Q_0/2$ because our target is only averaging the flux on the x-axis. For a similar reason, a thermal conductivity proportional to $\frac{1}{1-\sin\psi}$ is enough, so we can obtain Eq. (5):

$$\kappa(x,y) = \frac{\kappa_0}{1-\sin\psi(x,y)} = \kappa_0\left(1 + \sqrt{\frac{\left(x^2+y^2-1\right)^2}{x^4+2x^2\left(y^2+1\right)+\left(y^2-1\right)^2}}\right)^{-1}. \tag{S19}$$

The range of normalized thermal conductivity $\frac{\kappa_1}{\kappa_0}$ or $\frac{\kappa}{\kappa_0}$ is $[0.5, 1]$, and we illustrate their spatial distributions in Figs. S2(a) and S2(b).
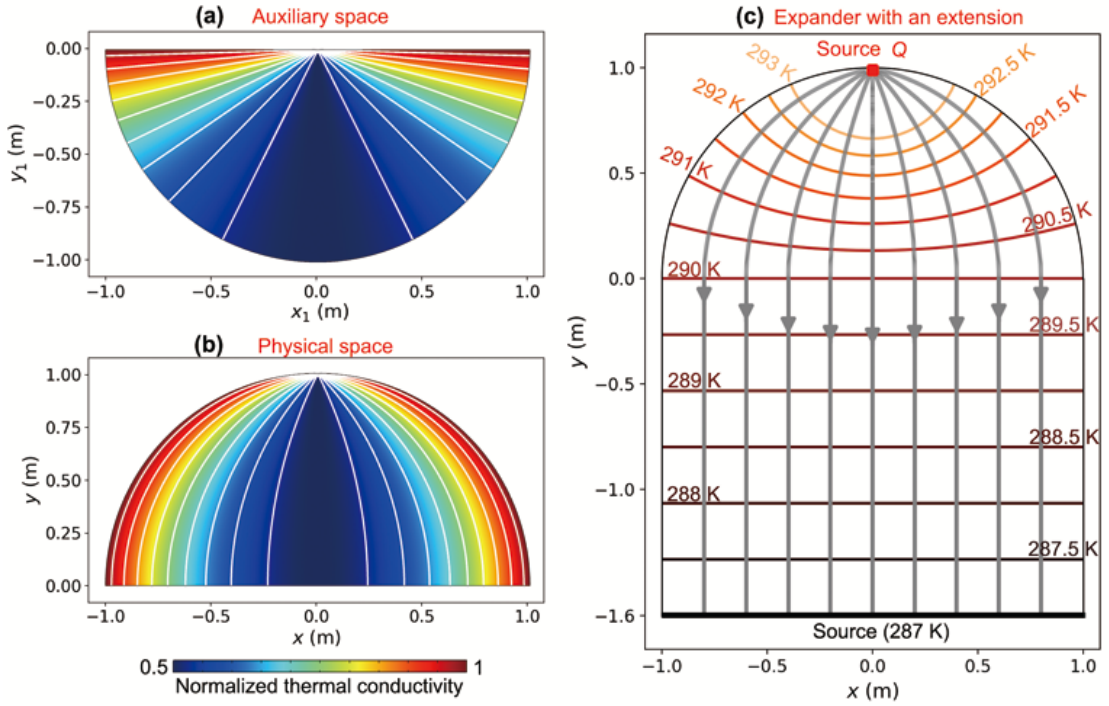

FIG. S2: Normalized thermal conductivity in the (a) auxiliary space and (b) physical space for the thermal expander. (c) Simulated temperature profile of the thermal expander with an extension.

Note IV: Thermal expander with an extension

Here, we give the performance of the thermal expander when an extension is attached to its bottom on the x-axis [Fig. S2(c)]. The extension region is a rectangle. Its height is 1.6 m in our simulation. The external heat source (thermostatic sink at 290 K) in Fig. 3(c) is removed now. Instead, another external source is put on the bottom of the extension, and its temperature is 287 K. The other boundaries of the whole system are all thermally insulated. The thermal conductivity in the extension is 400 W m^{-1} K^{-1}. Other parameters, including the point source power, are not changed. We plot the isotherms and streamlines in Fig. S2(c). We can see that the isotherms in the extension are all parallel to the x-axis and the streamlines are all parallel to the y-axis. This shows that the heat flux after parallelization by the expander can keep its direction in the extension. Here, the the extension's height and the source's temperature can have other values that do not influence the function of this expander. The value we set in the simulation can make the temperature on the x-axis exactly 290 K. Obviously, conformal mapping (Möbius transform) alone cannot keep the heat flux in the extension parallel to the x-axis under the boundary conditions in this case.

Note V: An alternative approach to thermal expander using transposed bipolor coordinates

Actually, we can see the contours in Fig. S2(b) (and the isobars and streamlines in Figs. 3(b) and 3(c)) have the same pattern as the grid lines for the bipolar coordinates. We can also use such a coordinate system in the physical space to obtain the thermal conductivity distributions in Eq. (5). Here, we use different definitions from the common bipolar coordinates. The two foci F_1 and F_2 of the bipolar coordinate system are placed on the y-axis of the Cartesian coordinate system, i.e., $(0, -1)$ and $(0, 1)$ [Fig. S3(a)]. The σ-coordinate of a point P, whose value range is $(-\pi, \pi)$, is related to the F_1PF_2 angle denoted by $\alpha \in (0, \pi]$. For a point in the left half-plane, e.g., A in Fig. S3(a), we take $\sigma = \alpha - \pi$ so it has a negative value. On the other hand, a point like B in the right half-plane has a positive σ value equal to $\pi - \alpha$. The τ-coordinate is defined by $\ln \frac{d_1}{d_2}$, in which d_1 and d_2 are the distance to F_1 and F_2, respectively. In Fig. S3(b), we plot some grid lines of this bipolar coordinate system. Both the curves of constant-σ and constant-τ are non-concentric circles,
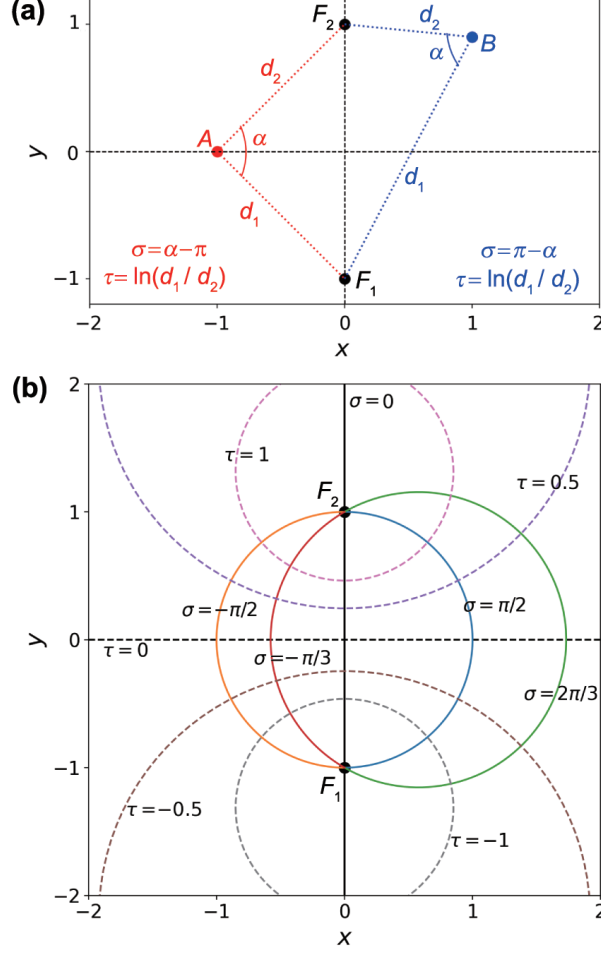
FIG. S3: (a) Schematic diagram for the definition of a transposed bipolar coordinate system with foci at $(0, \pm 1)$. (b) Curves of constant-σ (solid lines) and constant-τ (dashed lines).

except for $\sigma = 0$ (the y-axis) and $\tau = 0$ (the x-axis). In particular, curves of constant-σ and constant-$(\sigma - \pi)$ are on the same circle if $\sigma > 0$. It is easy to check that the scale factors of the two coordinates are the same, i.e., $h_\sigma = h_\tau = \frac{1}{\cosh \tau - \cos \sigma}$, so the heat conduction equation can be written as

$$(\cosh \tau - \cos \sigma)^2 \left(\kappa(\sigma) \frac{\partial^2 T(\tau)}{\partial \tau^2} \right) = 0 \tag{S20}$$

if $\frac{\partial T}{\partial \sigma} = 0$ and $\frac{\partial \kappa}{\partial \tau} = 0$. In other words, the temperature still satisfies a Laplace equation. This is just the case shown in Fig. 3 and Fig. S2, and we can find

$$\begin{cases} \tau = -\ln r \\ \sigma = \psi - \frac{3}{2}\pi \end{cases} \tag{S21}$$

12

under the Möbius transformation

$$x + iy = \tan\left(\frac{\sigma + i\tau}{2}\right) = i\frac{i + re^{i\psi}}{i - re^{i\psi}}. \tag{S22}$$

Similarly, the heat flux along the curve of constant-σ is

$$\kappa(\sigma)\frac{\partial T(\tau)}{\partial \tau}\left(\cosh \tau - \cos \sigma\right). \tag{S23}$$

To eliminate the difference of flux magnitude on the x-axis in the physical space, we should let

$$\kappa(\sigma) \sim \frac{1}{\cosh(\tau = 0) - \cos \sigma} = \frac{1}{1 - \cos \sigma} = \frac{1}{1 - \sin \psi}. \tag{S24}$$

We can see Eq. (S24) gives the same result as Eq. (5) and Eq. (S19), and κ can be written in a more compact form using the transposed bipolar coordinates.

Note VI: Inversion of the Zhukovsky transform and its branch cut

The general Zhukovsky transform [10]

$$z_1 = z + \frac{c^2}{4z} \tag{S25}$$

is conformal except for a simple pole $z = 0$ and can be used to map an annulus to an ellipse region (including the boundaries). In particular, the inner circle (with a radius equal to $c/2$) of the annulus is transformed into the line segment between the foci $(\pm c, 0)$ of the ellipse. It is easy to find that Eq. (S25) is not an injection due to $z_1(z) = z_1(c^2/4z)$. To make $z_1(z)$ a univalent function, we should consider the domain in which z and $c^2/4z$ cannot coexist, e.g., $\{z : |z| > c/2\}$ or $\{z : |z| < c/2\}$. The inverse map is thus a double-valued function [10]:

$$z = \frac{z_1 \pm \sqrt{z_1^2 - c^2}}{2} \tag{S26}$$

except at the algebraic branch points $(\pm c, 0)$. We should notice that the sign of $\pm$ in Eq. (S26) does not directly distinguish the two univalent branches of the inverse map. In fact, the two branches should conformally map the two sheets of the Riemann surface of the inverse map onto $\{z : |z| \geqslant c/2\}$ and $\{z : |z| \leqslant c/2\}$, respectively [10]. In addition, the line segment $[-c, c]$ (also called the branch cut) on the x_1-axis is mapped onto the circle $\{z : |z| = c/2\}$ by both branches.
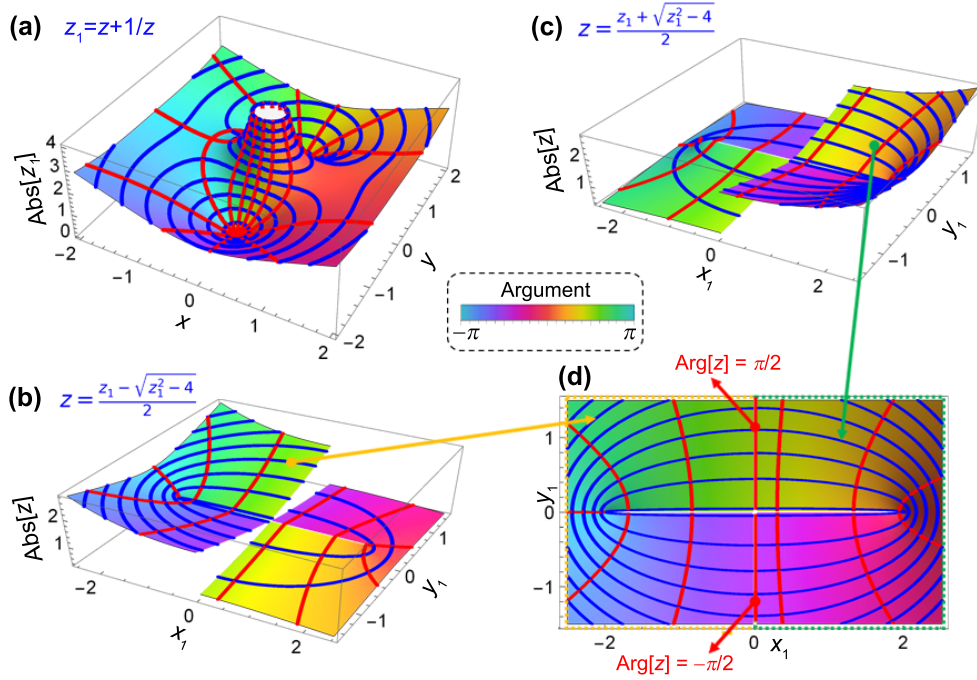
FIG. S4: The complex three-dimensional (3D) plot of Abs colored by Arg for (a) the Zhukovsky transform $z_1 = z + \frac{1}{z}$, (b) the inverse transform $z = \frac{z_1 + \sqrt{z_1^2 - 4}}{2}$, and (c) the inverse transform $z = \frac{z_1 - \sqrt{z_1^2 - 4}}{2}$. The red grid lines and the blue ones are isosurfaces of the argument and the absolute value of the corresponding images, respectively. (d) The projection (top view) of joined upper surfaces in (b) and (c).

For simplicity, we take $c = 2$ and illustrate the Zhukovsky transform and its inversion in Fig. S4. In Figs. S4(a)–S4(c), the height of the surface represents the absolute value (denoted by Abs) of the complex number, while the color represents the argument (denoted by Arg). We can see the two images of the inverse transformation shown in Figs. S4(b) and S4(c) are both split by the y_1-axis, demonstrating a discontinuity of Abs$[z]=|z|$. It is easy to check that both the upper surfaces in Figs. S4(b) and S4(c) correspond to the mapping onto the region exterior to the circle $\{z : |z| = c/2\}$ while the lower ones correspond to the map onto its interior. In addition, we can see the limits to the split edge has the relationship:

$$\lim_{x_1 \to 0^-} \frac{z_1 - \sqrt{z_1^2 - c^2}}{2} = \lim_{x_1 \to 0^+} \frac{z_1 + \sqrt{z_1^2 - c^2}}{2} = \frac{iy_1 + \sqrt{(iy_1)^2 - c^2}}{2}. \tag{S27}$$

Therefore the two upper surfaces can be joined along the y_1-axis on which the image takes the value of $\frac{z_1 + \sqrt{z_1^2 - c^2}}{2}$. Their projection, shown by a 2D plot in Fig. S4(d), can cover the whole complex plane. This represents one sheet of the Riemann surface to be mapped onto

14

$\{z : |z| \geqslant c/2\}$. In particular, an ellipse whose foci are also $(\pm c, 0)$ is transformed into an annulus, which gives (the outer layer of) the bilayer shell cloak and its carpet counterpart [Fig. 4]. Similarly, the two lower surfaces in Figs. S4(b) and S4(c) can also be joined, representing another sheet of the Riemann surface, to be mapped onto the area inside the cloak, i.e., $\{z : |z| \leqslant c/2\}$.

Note VII: Verification for transient cloaking

When considering transient heat conduction, Eq. (2) should be modified as

$$\rho C \frac{\partial T}{\partial t} - \nabla \cdot (\boldsymbol{\kappa} \nabla T(z)) - Q = 0, \tag{S28a}$$

$$\rho_0 C_0 \frac{\partial T_0}{\partial t} - \nabla_0 \cdot (\boldsymbol{\kappa}_0 \nabla_0 T_0(z_0)) - Q_0 = 0, \tag{S28b}$$

where t is the time, ρ and C are the density and the specific heat in the physical space, respectively, and ρ_0 and C_0 are their counterparts in the virtual space. They satisfy [11]

$$\rho(z)C(z) = \rho_0(z_0)C_0(z_0)/\det \mathrm{J}_f. \tag{S29}$$

Therefore, a steady-state cloak is distinguished from a transient cloak in that the product of density and specific heat also affects heat transfer in the latter. In order to apply the same transformation as the steady state, the streamlines and isotherms at each moment in the virtual space should be the grid lines of the Cartesian coordinate system. In this way, Eq. (S13) should induce the same thermal conductivity as the cloak for steady conduction [Eq. (7) or Eq. (8)]. A common situation is to make the temperature uniform at the initial moment, such as at the temperature of the cold source. Fig. S5 shows the simulated temperature at different times for both the normal bilayer cloak and zero-index cloak. We use the same material and boundary settings as in Fig. 4 and take $\rho_0 = 8900$ kg m^{-3} and $c_0 = 385$ J kg^{-1} K^{-1}. The value of $\det \mathrm{J}_f$ is

$$\det \mathrm{J}_f = \frac{ab}{R_2^2} \left| \frac{\mathrm{d}z}{\mathrm{d}z_1} \right|^2 = \frac{R_2^4 - R_1^4}{R_2^4} \frac{(x^2 + y^2)^2}{((x + R_1)^2 + y^2)((x - R_1)^2 + y^2)}. \tag{S30}$$

In previous studies [12], a normal bilayer cloak without transforming the density or specific heat will noticeably lose its invisibility in transient situations, especially when the isotherms are centered near the heat source, i.e., far from the nonequilibrium steady state.
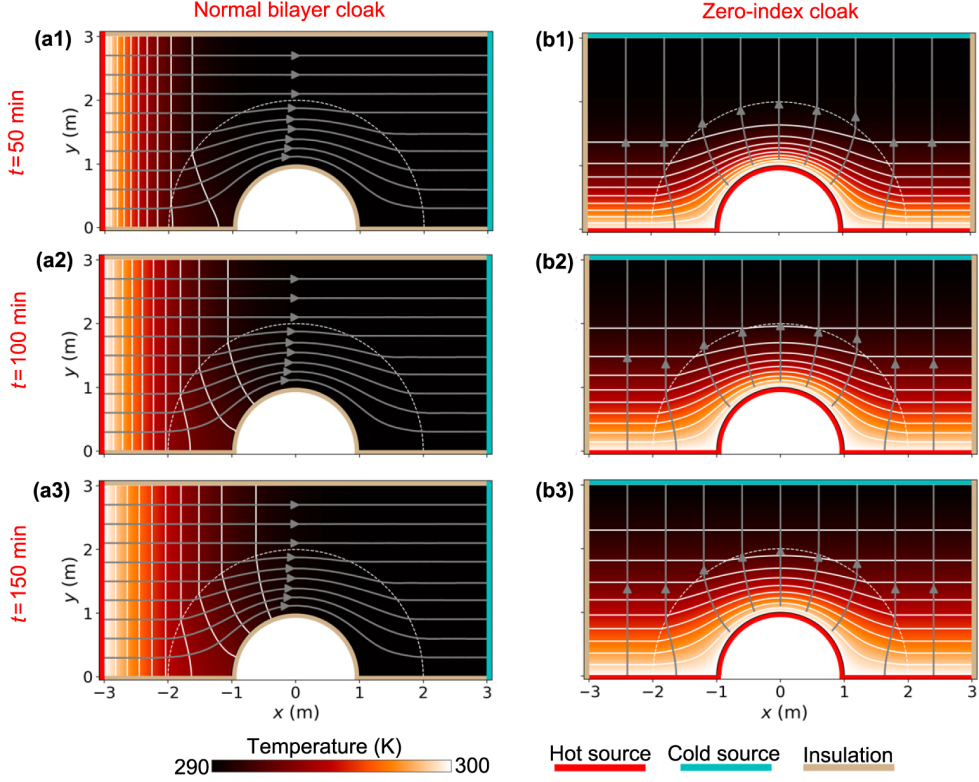
FIG. S5: Simulated temperatures at different times (50 min, 100 min and 150 min). (a1)–(a3) are the results for normal bilayer cloak while (b1)–(b3) are the results for zero-index cloak. The white dotted lines frame the inner layer of the cloaks. Same as Fig. 4, the white solid curves indicate isotherms (from 291 K to 299 K with an interval of 1 K), and the gray solid curves with arrows represent streamlines. The initial temperature distribution is 290 K for the whole domain.

In Figs. S5(a1)–(a3), we can see the cloaking and invisibility effect is perfect at each moment when introducing a spatial gradient of density times specific heat. The "carpet" or semi-annulus zero-index cloak also perform well [Figs. S5(b1)–(b3)]. In the transient case, the lower boundary, including the so-called inner layer, is still an isotherm with a constant value. For the complete "shell" cloak, the boundary condition on the inner layer (central circle whose radius is R_1) needs to be set as an isotherm whose temperature value varies over time. It is easy to see the time-dependent value is equal to the reference temperature at the center (x–axis) of the virtual space.
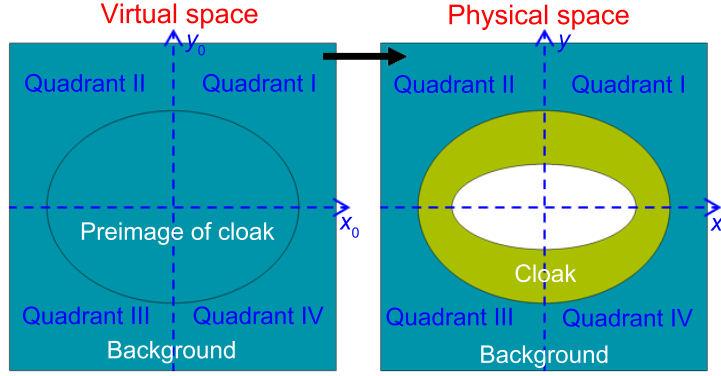
FIG. S6: Schematic illustration of the transformation to get a confocally elliptical shell cloak. The ellipse in the virtual space (preimage of the cloak) is mapped onto the shell cloak in the physical space. The background outside the cloak undergoes an identity transformation.

Note VIII: Confocally elliptical shell cloak

In addition to annular cloaks, the method of pseudo-conformal mapping can also be used to design cloaks with other geometries like confocal ellipses. Take the shell cloak as an example (referring to the outer layer of a bilayer cloak). We need to transform an ellipse into a shell whose boundaries are confocal elliptical loops [Fig. S6]. Their common foci are denoted by $(\pm c, 0)$ on the x-axis. The definition of the elliptic coordinates (μ, ν) in the physical space can be expressed as

$$z = x + iy = c \cosh(\mu + i\nu) = c\frac{e^{\omega} + e^{-\omega}}{2}, \tag{S31}$$

where $\omega = \mu + i\nu$ (μ is a nonnegative real number and $\nu \in [0, 2\pi)$) is also a point in the complex plane. This relationship actually shows a Zhukovsky transform $e^{\omega} \mapsto z$ with a coefficient $c/2$. It is worth noting that, in Fig. S4(d), the curves of constant-$|z|$ are just elliptical loops with the same foci. In other words, the Zhukovsky transform can map concentric circles to confocal elliptical loops.

Inspired by Eq. (S31), we use the following transformation to construct an elliptical shell cloak [Fig. S7]. For simplicity, we take $c = 2$ and only consider the map in Quadrant I. The μ coordinates of the cloak's inner and outer elliptical boundaries are μ_1 and μ_2, respectively. We start from the virtual space [Fig. S7(a)]. The upper-right quarter-ellipse domain has a semi-major axis equal to $2 \cosh \mu_2$ and a semi-minor axis equal to $2 \sinh \mu_2$. We should finally transform it onto the area wrapped by elliptical loops denoted by μ_1 and μ_2 in the physical
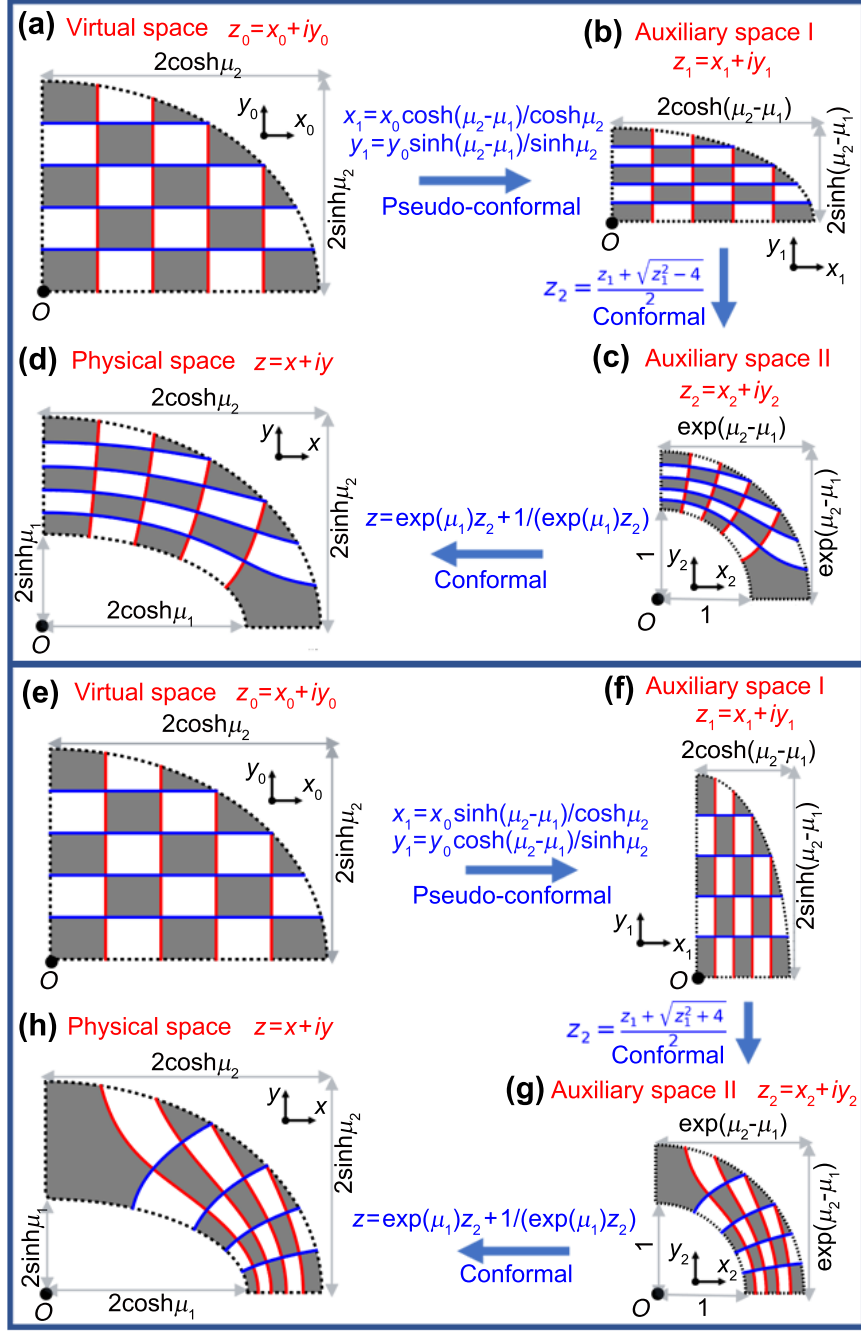
17

FIG. S7: The 3-step transformation to design a confocally elliptical cloak. Only the part in Quadrant I is illustrated. (a)–(d) The procedure to obtain a normal bilayer cloak when the thermal bias is applied along the x-axis or a zero-index cloak when the thermal bias is applied along the y-axis. (e)–(f) The procedure to obtain a zero-index cloak when the thermal bias is applied along the x-axis or a normal bilayer cloak when the thermal bias is applied along the y-axis.

space [Fig. S7(d)]. An intermediate target can be an upper-right quarter-annulus, and then

we can use a Zhukovsky-like transform to get the cloak. The map onto the quarter-annulus can be decomposed into two steps. First, do a compression

$$\begin{cases} \dfrac{x_1}{x_0} = \dfrac{\cosh(\mu_2 - \mu_1)}{\cosh \mu_2} \\ \dfrac{y_1}{y_0} = \dfrac{\sinh(\mu_2 - \mu_1)}{\sinh \mu_2} \end{cases} \tag{S32}$$

from Figs. S7(a) to S7(b), whose image in the auxiliary space I is another quarter-ellipse with a semi-major axis equal to $2\cosh(\mu_2 - \mu_1)$ and a semi-minor axis equal to $2\sinh(\mu_2 - \mu_1)$. Second, like what we have done in designing the annular cloak, use the second branch of Eq. (6) to obtain the quarter-annulus in the auxiliary space II, whose outer and inner radii are $e^{\mu_2 - \mu_1}$ and 1, respectively. Finally, the Zhukovsky-like transform

$$z = e^{\mu_1} z_2 + \left(e^{\mu_1} z_2 \right)^{-1} \tag{S33}$$

shapes the confocally elliptical cloak in Quadrant I. Its counterpart in Quadrant IV can be generated by the same procedure. To obtain the left part of the cloak in Quadrant II and III, we should use the first branch of Eq. (6) instead. The whole transformation from Figs. S7(a) to S7(d) for the shell cloak again demonstrates a topological genus change that maps the line segment $\{z_0 : -\frac{2\cosh \mu_2}{\cosh(\mu_2 - \mu_1)} \leqslant x_0 \leqslant \frac{2\cosh \mu_2}{\cosh(\mu_2 - \mu_1)}, y_0 = 0\}$ to the elliptical loop denoted by elliptic coordinate μ_1. Also, two solutions for cloaking can be found here. If the thermal bias is applied along the x-axis, we should set the shell's thermal conductivity and the boundary condition on the elliptical loop μ_1 as

$$\begin{cases} \kappa = \kappa_0^{x_0 x_0} \dfrac{\partial x_1}{\partial x_0} \dfrac{\partial y_0}{\partial x_1} = \kappa_0^{x_0 x_0} \tanh \mu_2 \coth(\mu_2 - \mu_1) \\ \kappa(\mu = \mu_1) = 0. \end{cases} \tag{S34}$$

On the other hand, if the thermal bias is along the y-axis, we will get the zero-index cloak, which requires

$$\begin{cases} \kappa = \kappa_0^{y_0 y_0} \dfrac{\partial y_1}{\partial y_0} \dfrac{\partial x_0}{\partial x_1} = \kappa_0^{y_0 y_0} \coth \mu_2 \tanh(\mu_2 - \mu_1) \\ T(\mu = \mu_1) = T_0(y_0 = 0). \end{cases} \tag{S35}$$

Different from the symmetry of an annular cloak, turning a line segment on the y_0-axis into an elliptical loop will yield another set of solutions. The procedure in Figs. S7(e)–S7(h) shows such a transformation, and we change the first two mappings compared with Figs. S7(a)–S7(d). First, we need a mapping to move the foci to the y_1-axis, which can be
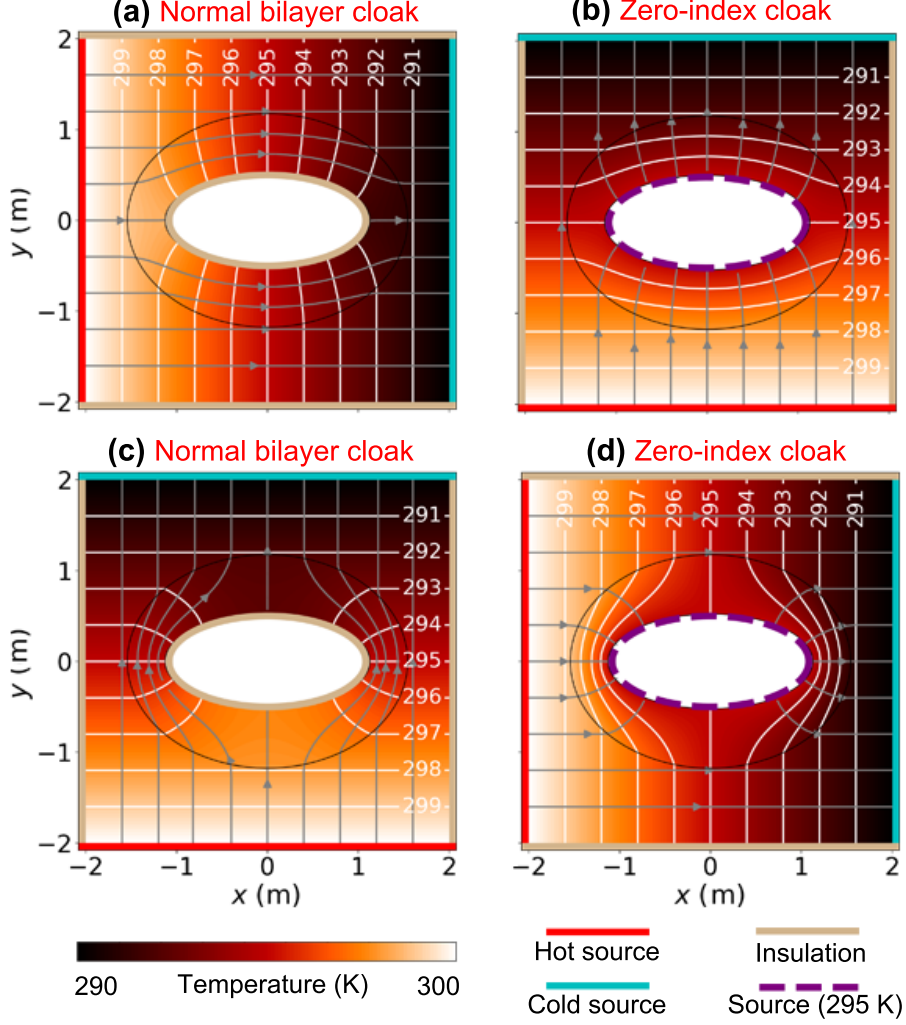
19

FIG. S8: Temperature profiles for elliptical cloaks with the same geometry. (a) The normal bilayer cloak under a thermal bias along the x-axis. Its inner layer, plotted by a brown elliptical loop, is thermally insulated. The thermal conductivity in its outer layer (the shell with confocally elliptical boundaries) is given by Eq. (S34). (b) The zero-index cloak under a thermal bias along the y-axis. The inner layer, indicated by a purple dashed curve, has a constant temperature maintained by an external source. The thermal conductivity in its outer layer is given by Eq. (S35). (c) The normal bilayer cloak under a thermal bias along the y-axis. Its inner layer is thermally insulated. The thermal conductivity in its outer layer is given by Eq. (S38). (d) The zero-index cloak under a thermal bias along the x-axis. The inner layer has a constant temperature maintained by an external source. The thermal conductivity in its outer layer is given by Eq. (S39).

20

realized by the compression transformation [Figs.S7(e) and S7(f)]

$$\begin{cases} \dfrac{x_1}{x_0} = \dfrac{\sinh(\mu_2 - \mu_1)}{\cosh \mu_2} \\ \dfrac{y_1}{y_0} = \dfrac{\cosh(\mu_2 - \mu_1)}{\sinh \mu_2}. \end{cases} \tag{S36}$$

Then, the conformal map onto an annulus that replaces Eq. (6) is

$$\begin{cases} z_2 = \dfrac{z_1 - \sqrt{z_1^2 + 4}}{2}, & \text{if } x_1 < 0 \\ z_2 = \dfrac{z_1 + \sqrt{z_1^2 + 4}}{2}, & \text{if } x_1 \geqslant 0. \end{cases} \tag{S37}$$

The second formula is used to obtain the upper-right quarter-annulus in Fig.S7(g). In fact, Eq. (S37) is one branch of the inversion of $z_1 = z_2 - 1/z_2$. The last step to Fig.S7(h) is still using Eq. (S33), and the 3-step procedure finally maps the line segment $\{z_0 : -\frac{2\sinh\mu_2}{\cosh(\mu_2-\mu_1)} \leqslant y_0 \leqslant \frac{2\sinh\mu_2}{\cosh(\mu_2-\mu_1)}, x_0 = 0\}$ onto the inner elliptical loop denoted by μ_1. Similarly, we can see the normal bilayer-cloak solution is

$$\begin{cases} \kappa = \kappa_0^{y_0 y_0} \coth \mu_2 \coth(\mu_2 - \mu_1) \\ \kappa(\mu = \mu_1) = 0 \end{cases} \tag{S38}$$

when the thermal bias is put along the y-axis. The zero-index-cloak solution is

$$\begin{cases} \kappa = \kappa_0^{x_0 x_0} \tanh \mu_2 \tanh(\mu_2 - \mu_1) \\ T(\mu = \mu_1) = T_0(x_0 = 0) \end{cases} \tag{S39}$$

when the thermal bias is put along the x-axis. The solutions given by Eq. (S34) and (S38) have been obtained in Refs. [13, 14] by solving the heat equation directly. Here we give a geometric approach to get the same material parameters and find another set of cloaking condition [Eqs. (S35) and (S39)] related to the zero-index cloak with confocal elliptical configuration. It is worth noting that the elliptical cloak has one more pair of invisibility conditions than the annular cloak because it no longer has the symmetry of the 90° rotation.

As an example, we take $\mu_1 = 0.5$, $\mu_2 = 1$ and $\kappa_0 = 400$ W m^{-1} K^{-1}, and show the performance of these four cloaks in Fig. S8 based on finite element modeling. The values of the corresponding hyperbolic functions and the focal length $2c$ are measured in meters. The geometry of the whole system is a square with the center at the origin and a side length of 4 m. The thermal bias is 10 K, achieved by a hot source fixed at 300 K (represented by a thick red solid line) and a cold source fixed at 290 K (represented by a thick cyan

solid line). Figs. S8(a), S8(b), S8(c), and S8(d) represent the cloak based on Eq. (S34), Eq. (S35), Eq. (S38), and Eq. (S39), respectively. Figs. S8(a) and S8(c) are normal bilayer cloaks whose inner layers are drawn in brown as well as other boundaries with thermal insulation conditions. Figs. S8(b) and S8(d) are zero-index cloaks. Purple dashed lines represent their inner layers, and a constant temperature of 295 K is set on them. 295 K is just the temperature on the x_0-axis in the virtual space. All four cloaks show a perfect invisibility effect. The duality relationship of the isotherms and the streamlines can also be observed between Figs. S8(a) and S8(b) or between Figs. S8(c) and S8(d).

---

[1] L. V. Ahlfors, *Lectures on Quasiconformal Mappings*, 2nd. (American Mathematical Society, Providence, 2006).

[2] V. Alberge and A. Papadopoulos, in *Handbook of Teichmüller Theory, Volume VII*, edited by A. Papadopoulos (European Mathematical Society, Zürich, 2020), pp. 393–415.

[3] J. Li and J. B. Pendry, Phys. Rev. Lett. **101**, 203901 (2008).

[4] R. Liu, C. Ji, J. J. Mock, J. Y. Chin, T. J. Cui, and D. R. Smith, Science **323**, 366 (2009).

[5] B. Zhang, T. Chan, and B.-I. Wu, Phys. Rev. Lett. **104**, 233903 (2010).

[6] J. Zhang, J. B. Pendry, and Y. Luo, Adv. Photonics **1**, 014001 (2019).

[7] W. Zeng, L. M. Lui, F. Luo, T. F.-C. Chan, S.-T. Yau, and D. X. Gu, Numer. Math. **121**, 671 (2012).

[8] E. M. Stein and R. Shakarchi, *Complex Analysis* (Princeton University Press, Princeton, 2003).

[9] V. A. Markel, J. Opt. Soc. Am. A **33**, 1244 (2016).

[10] J. W. Brown and R. V. Churchill, *Complex Variables and Applications*, 9th. (McGraw-Hill Education, New York, 2014).

[11] S. Guenneau, C. Amra, and D. Veynante, Opt. Express **20**, 8207 (2012).

[12] T. Han, X. Bai, D. Gao, J. T. L. Thong, B. Li, and C.-W. Qiu, Phys. Rev. Lett. **112**, 054302 (2014).

[13] T. Han, P. Yang, Y. Li, D. Lei, B. Li, K. Hippalgaonkar, and C.-W. Qiu, Adv. Mater. **30**, 1804019 (2018).

[14] J. Qin, W. Luo, P. Yang, B. Wang, T. Deng, and T. Han, Int. J. Heat Mass Transfer **141**, 487 (2019).